

Activity-Driven Local ATP Synthesis Is Required for Synaptic Function

Vidhya Rangaraju,^{1,2} Nathaniel Calloway,² and Timothy A. Ryan^{2,*}

¹Rockefeller/Sloan-Kettering/Weill Cornell Tri-Institutional Training Program in Chemical Biology, New York, NY 10065, USA

²Department of Biochemistry, Weill Cornell Medical College, New York, NY 10065, USA

*Correspondence: taryan@med.cornell.edu

<http://dx.doi.org/10.1016/j.cell.2013.12.042>

SUMMARY

Cognitive function is tightly related to metabolic state, but the locus of this control is not well understood. Synapses are thought to present large ATP demands; however, it is unclear how fuel availability and electrical activity impact synaptic ATP levels and how ATP availability controls synaptic function. We developed a quantitative genetically encoded optical reporter of presynaptic ATP, *Syn-ATP*, and find that electrical activity imposes large metabolic demands that are met via activity-driven control of both glycolysis and mitochondrial function. We discovered that the primary source of activity-driven metabolic demand is the synaptic vesicle cycle. In metabolically intact synapses, activity-driven ATP synthesis is well matched to the energetic needs of synaptic function, which, at steady state, results in $\sim 10^6$ free ATPs per nerve terminal. Despite this large reservoir of ATP, we find that several key aspects of presynaptic function are severely impaired following even brief interruptions in activity-stimulated ATP synthesis.

INTRODUCTION

Changes in global metabolic state, particularly starvation and insulin-induced hypoglycemia are known to have profound effects on cognitive function. This is generally attributed to the fact that the central nervous system consumes $\sim 20\%$ of energy in the body using glucose as its main source of fuel. Within the brain, synapses are, in turn, thought to be primary sites of ATP consumption (Harris et al., 2012). In many cells, metabolic pathways are well known to contain multiple levels of feedback control to maintain cellular ATP. Presynaptic terminals are expected to place high ATP demands on energy supplies when they are active as they rely on numerous ATPases such as Na^+/K^+ , H^+ , and Ca^{2+} pumps, as well as different protein disassembly machineries (AAA ATPases, HSC70/auxilin) for continuous operation (Ly and Verstreken, 2006). Functional neuronal states are generally defined in terms of whether or not they are electrically active and firing action potentials (APs). Synaptic activity is expected to vary greatly over time and energy demands must be

met locally as nerve terminals are found at great distances from cell bodies. Additionally, mitochondrial dysfunction has been implicated in numerous neurological disorders, but the significance of this with regard to synaptic function is unknown as several basic features of synaptic metabolism have remained uncharted, including: (1) how electrical activity impacts presynaptic ATP levels; (2) how changes in ATP-synthesis pathways impact synaptic ATP levels; (3) what aspect of synapse function places burdens on energy supplies; and (4) how changes in ATP levels and supply routes, in turn, impact synaptic function. The difficulty in predicting relative sensitivities of synapse function to alterations in ATP synthesis routes arises from the paucity of information about the relevant in vivo K_m values for ATP binding of the proteins and enzymes supporting synapse function and how these K_m values compare to intracellular synaptic ATP levels. Approaching such questions requires quantitative measures of ATP levels in nerve terminals. Here, we report the development of a quantitative, ratiometric optical reporter of presynaptic ATP concentration ($\text{ATP}_{\text{presyn}}$), and its use to examine ATP dynamics, regulation, and consumption at nerve terminals.

RESULTS

A Quantitative Reporter of Presynaptic ATP

Previous optical reporters of ATP have suffered from a number of drawbacks for attacking this problem, including nonlinearity (Imamura et al., 2009; Saito et al., 2012), saturation at expected physiological ATP levels (Berg et al., 2009; Tantama et al., 2013), and sensitivity to other nucleotides such as ADP making them unsuitable for quantitative measures of ATP. Firefly luciferase catalyzes the oxidation of luciferin, a cell-permeant substrate, using ATP and Mg^{2+} to give light with a quantum yield of 0.41 (Fraga, 2008). This enzymatic process specifically requires ATP and other nucleotides do not impact this protein's function (Moyer and Henderson, 1983), thereby making luciferase an efficient optical reporter of ATP. However, two major limitations hamper its use for quantitative subcellular imaging: its slow catalytic rate ($k_{\text{cat}} = 1.6 \text{ s}^{-1}$) (Branchini et al., 1998) and lack of a suitable calibration for specific activity in situ. Bioluminescence, however, has intrinsically high sensitivity owing to the absence of background signals. Expression of cytosolic wild-type (WT) luciferase in hippocampal neurons bathed in luciferin nonetheless resulted in luminescence images with very low signal-to-noise ratios where presynaptic terminals could not be clearly distinguished even with prolonged integration times using

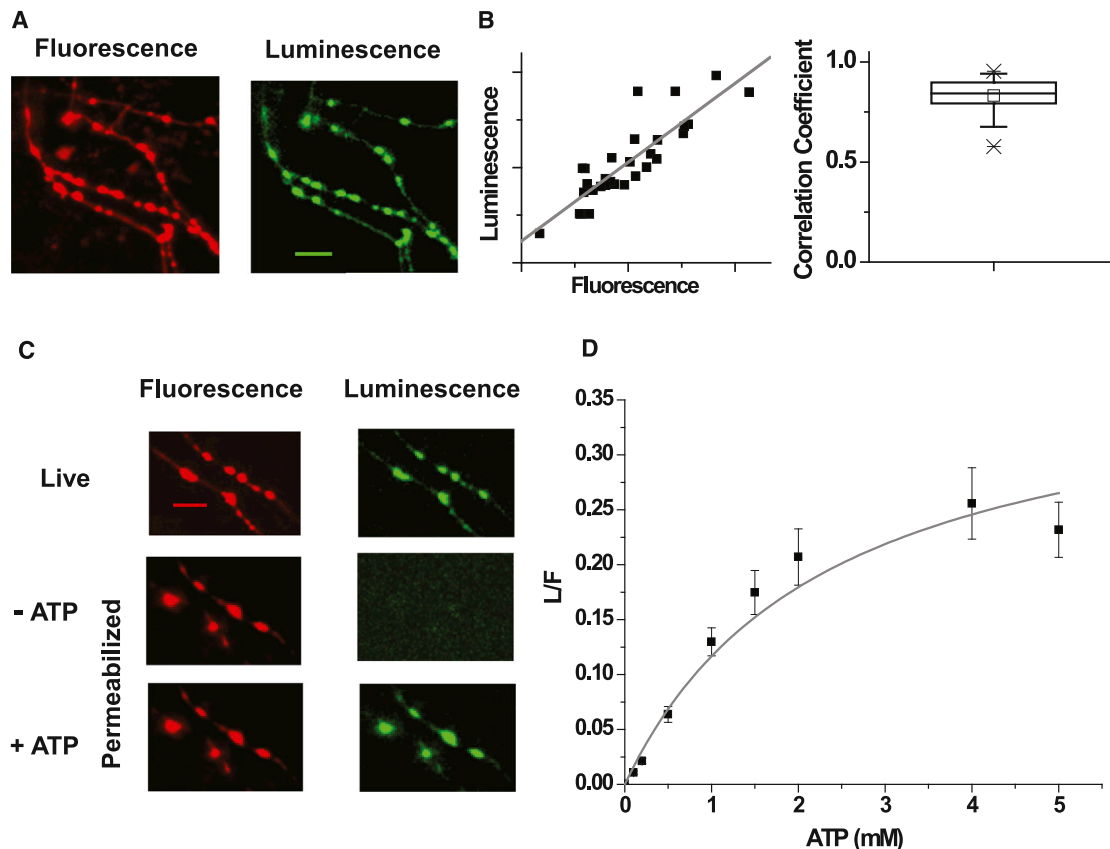


Figure 1. Syn-ATP: A Genetically Encoded ATP Reporter

(A) Fluorescence (red) and luminescence (green) images of Syn-ATP in the presence of 2 mM luciferin expressed in hippocampal neurons. Scale bar, 10 μ m. (B) Correlation between individual bouton luminescence and fluorescence intensities from a sample experiment (left). Average correlation coefficient measured across cells = 0.83 ($n = 50$) (right). The box whisker plot represents median (line), mean (point), 25th–75th percentile (box), 10th–90th percentile (whisker), 1st–99th percentile (X), and min-max (–) ranges.

(C) Fluorescence (red) and luminescence (green) images acquired before (top) and after (middle) permeabilization in the presence of luciferin, followed by addition of ATP (bottom). Scale bar, 10 μ m.

(D) ATP titration curve of Syn-ATP fit with Michaelis-Menten relationship yielding K_m (ATP) = 2.3 ± 0.6 mM, $n = 10$.

Error bars are SEM. See also [Figures S1](#) and [S2](#).

high-sensitivity collection optics ([Figure S1A](#) available online). In order to improve the signal at nerve terminals, we took advantage of subcellular targeting by fusing luciferase to the C-terminal of the synaptic vesicle protein synaptophysin ([Granseth et al., 2006](#)). To calibrate the local photon flux in terms of the number of luciferase enzymes present, luciferase was tagged with the pH-, thermo-, and photo-stable fluorescent protein mCherry ([Shaner et al., 2005](#)), thereby allowing ratiometric luminescence to fluorescence (L/F) readouts. Expression of this chimeric ATP reporter ([Figure S1B](#)) in hippocampal neurons led to efficient delivery of functional luciferase at presynaptic terminals ([Figures 1A](#) and [S1C](#)), with limited impact on presynaptic function ([Figures S1D](#) and [S1E](#)), using 2 mM bath luciferin. Higher concentrations of luciferin were found to impair synaptic function ([Figures S1F–S1H](#)), and therefore all measurements were carried out at 2 mM. Luminescence and fluorescence signals were linearly correlated (average correlation coefficient = 0.83 ± 0.01 , $n = 50$; [Figure 1B](#)), and this approach provided much higher signal-to-noise imaging than cytosolic luciferase.

In order to calibrate the reporter to determine absolute ATP levels, we developed an in situ protocol for permeabilizing the plasma membrane using the hemolytic exotoxin, Streptolysin-O ([Martys et al., 1995](#)) (see [Experimental Procedures](#)). This exotoxin should create holes in the plasma membrane large enough to allow ATP to pass ([Figure S2A](#)). Application of Streptolysin-O abolished the luminescence signal but left the synaptic fluorescence signal relatively unperturbed ([Figure 1C](#)). Readdition of exogenous ATP restored the luminescence signal ([Figure 1C](#)). Thus, the system allowed for a simple systematic analysis of the reporter behavior in situ as a function of defined ATP concentration. Although WT luciferase permitted such calibrations at 30°C, at physiological temperatures in permeabilized synapses, the activity declined rapidly following addition of ATP ([Figure S2B](#)). Luciferase is known to be thermolabile and introduction of a set of five thermostabilizing mutations ([Branchini et al., 2007](#)) prevented loss of activity at 37°C in permeabilized synapses. We additionally incorporated two point mutations to increase luciferase's k_{cat} ([Fujii et al., 2007](#)) to further optimize

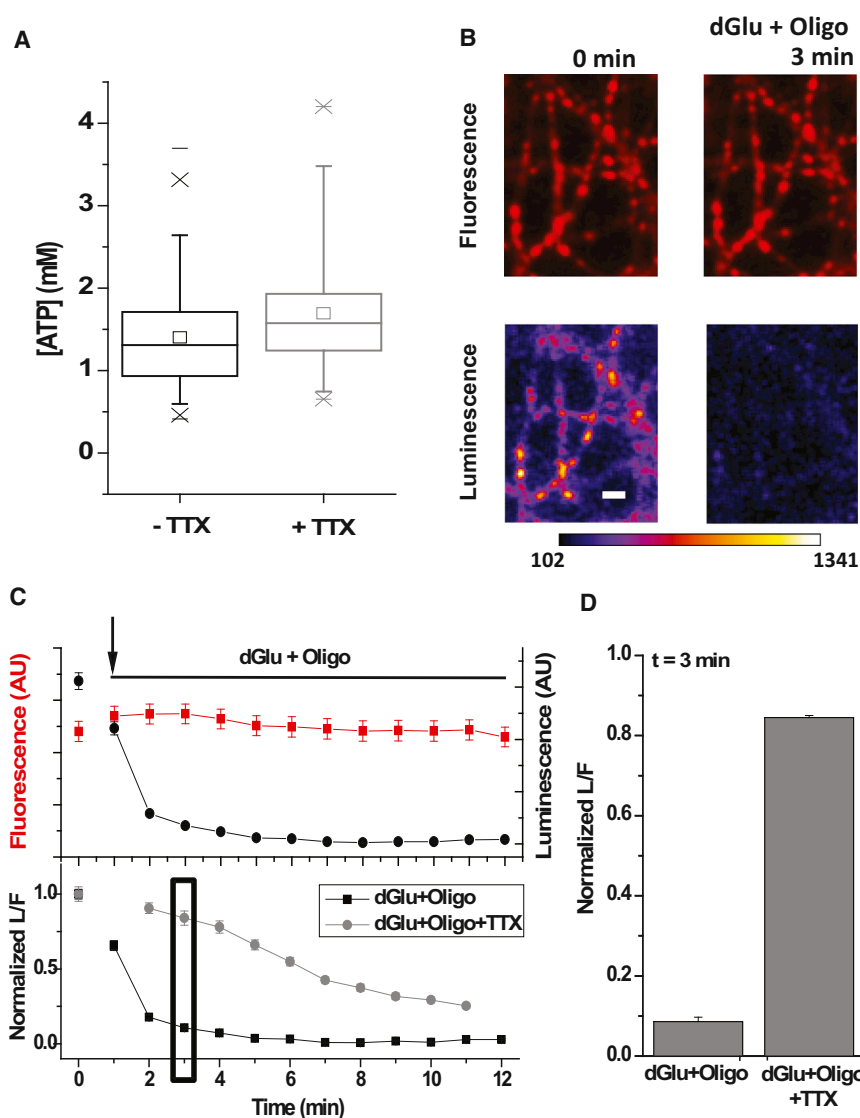


Figure 2. Activity Drives Large ATP Consumption

(A) Average ATP measured in neurons in the absence and presence of TTX. The box whisker plot represents median (line), mean (point), 25th–75th percentile (box), 10th–90th percentile (whisker), 1st–99th percentile (X), and min-max (–) ranges.

(B) Fluorescence and luminescence images acquired before and after 3 min incubation in deoxyglucose and oligomycin (dGlu+Oligo). Scale bar, 5 μ m. Pseudocolor intensity scales is in arbitrary units.

(C) Corresponding fluorescence, luminescence intensities (top), and L/F normalized to the initial resting L/F value measured during the time course of the experiment in comparison with dGlu+Oligo treatment in the presence or absence of TTX (bottom). The black rectangle highlights the 3 min time point.

(D) Average normalized L/F measured after 3 min incubation in dGlu+Oligo in the presence or absence of TTX (n = 4).

Error bars are SEM. See also Figure S3.

the reporter. We refer to the chimeric optimized ratiometric reporter as Syn-ATP. Systematic measurements of L/F of Syn-ATP as a function of applied ATP allowed us to construct an ATP titration curve (Figure 1D) that could be described with simple enzyme kinetics. Syn-ATP was insensitive to variations in Ca^{2+} , but the apparent K_m for ATP was modulated by pH ($\text{pK}_a = 7.03 \pm 0.04$) (Figures S2C–S2E), which likely arises in part from the protonation of ATP itself (De Stefano et al., 2006). This calibration allowed us to convert measurements of Syn-ATP's reported L/F (average L/F = 0.12 ± 0.003) along with parallel measurements of intracellular pH for intact synapses (Figures S3A–S3C, see Experimental Procedures) into $\text{ATP}_{\text{presyn}}$. These data show that under our standard recording conditions $\text{ATP}_{\text{presyn}} > 1.4$ mM (Figure 2A, absence of TTX) (averaged over 150 neurons, each providing 20–30 boutons, CV = 29%) which corresponds to $\sim 10^6$ molecules in a typical presynaptic varicosity (~ 1 fl). Only a small fraction of the apparent variations in $\text{ATP}_{\text{presyn}}$ across different cells could be attributed to possible

cell-to-cell variation in presynaptic intracellular pH (Figure S3B, Control). Although Syn-ATP itself consumes ATP, this burden is likely inconsequential as the total flux of photons corresponds to the consumption of only $\sim 2,300$ ATPs/min/synapse (see Experimental Procedures).

Activity Drives Large ATP Consumption

One of the most basic questions regarding synaptic metabolism is the degree to which electrical activity imposes significant ATP demands compared to basal metabolism. Although functional brain imaging (e.g., FDG-PET or fMRI) rely on the fact that region-specific neuronal activity drives local metabolic changes, it is difficult to quantitatively determine how this compares to baseline metabolism or to accurately attribute these changes to a particular cell type. We therefore examined how changes in chronic electrical activity impacted steady-state synaptic ATP levels. Chronic incubation of neurons in the Na^+ channel blocker Tetrodotoxin (TTX), which prevents action potential (AP) firing, led to only small changes in resting ATP levels (Figure 2A). Thus, either electrical activity does not impose significant additional metabolic burdens at synapses or increases in demand for ATP associated with electrical activity are accompanied by activity-driven increases in ATP synthesis. To distinguish between these two possibilities, we examined the kinetics of ATP decay in the presence or absence of TTX when all ATP synthesis was blocked. In the absence of TTX, the measured L/F values, which should be proportional to ATP levels, plummeted rapidly ($t_{1/2} \sim 2$ min, Figures 2B and 2C) in the presence of a combination of the glycolysis inhibitor 2-deoxyglucose (dGlu) and the $\text{F}_0\text{-F}_1$

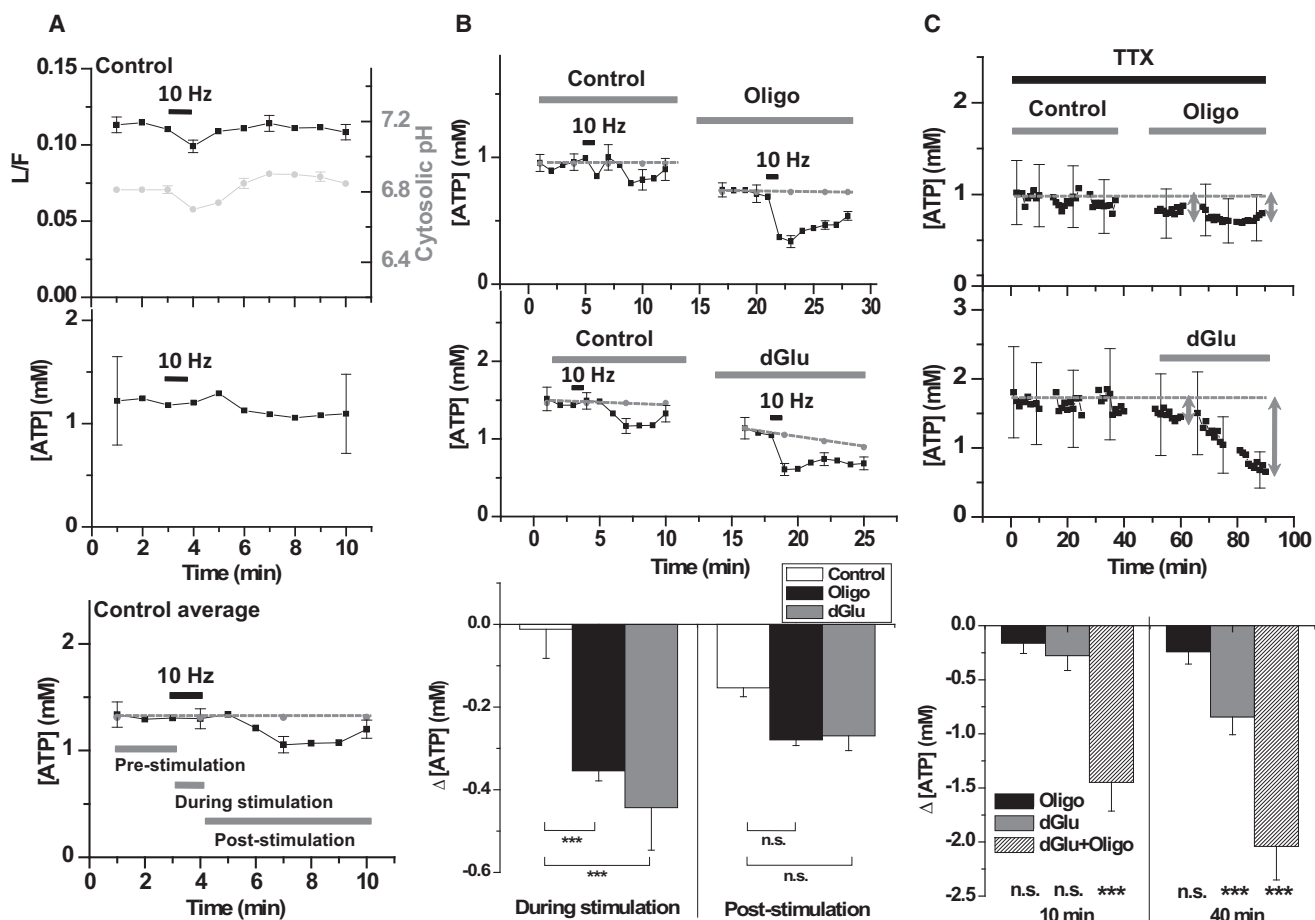


Figure 3. Stimulation Drives ATP Synthesis

(A) Representative L/F time course from a collection of 30 boutons from one neuron during a 60 s period of 10 Hz AP firing and separate cytoplasmic pHluorin based measurements of pH measured under the same condition, averaged across experiments ($n = 12$) (top), which was used to obtain a calibrated ATP time course (middle). ATP time course averaged across experiments ($n = 30$ cells) (bottom). Gray dotted line indicates baseline average of first 3 min during the prestimulation period; error bars are SEM.

(B) Average ATP time course measured pairwise in the absence and presence of Oligo ($n = 9$, top) or dGlu ($n = 21$, middle) during a 60 s period of 10 Hz AP firing. (Bottom) Average Δ ATP_{presyn} measured over the stimulus period (during stimulation) or averaged over 6 min after the stimulation (poststimulation) showed that ATP levels dropped significantly compared to control in dGlu ($p < 0.000001$) or in Oligo ($p = 0.0003$) during the stimulus period.

(C) Single neuron example of resting presynaptic ATP levels (ATP_{presyn}) in TTX in the absence or presence of Oligo (top) or dGlu (middle). Gray arrows indicate 10 and 40 min time points. Average drop in ATP (Δ ATP_{presyn}) measured after 10 min ($n = 5$ cells; $p = 0.64$, Oligo; $p = 0.27$, dGlu; $p < 0.000001$, Oligo+dGlu) or 40 min ($n = 5$ cells; $p = 0.35$, Oligo; $p = 0.0004$, dGlu; $p < 0.000001$, Oligo+dGlu) in Oligo, dGlu or a combination of both compared to the initial resting ATP level (bottom). Error bars are SEM. Error bars in (A) (middle) and (C) (top and middle) represent propagated error/uncertainty involved in [ATP] estimation (see [Experimental Procedures](#)). Student's t test was used to determine all the statistics. See also [Figure S3](#).

ATPase inhibitor oligomycin (Oligo). During the precipitous drop in ATP, changes in membrane excitability may exacerbate the metabolic decline. We found that the rate of ATP decay in these experiments was much slower in the presence of TTX ($t_{1/2} = 6 \pm 1$ min, [Figures 2C and 2D](#)), demonstrating that AP-driven synaptic function places very significant additional burdens on presynaptic ATP needs compared to basal metabolism. This result, together with the observation that chronic blockade of activity did not change ATP levels, implies that ATP synthesis must be driven by activity.

Activity Drives ATP Synthesis

Although the above experiments clearly demonstrate that the firing state of neurons has a large influence on ATP consumption,

the simple absence or presence of TTX is a relatively blunt tool for examining the impact of activity. We therefore examined ATP levels in synapses during defined bursts of electrical activity. We monitored Syn-ATP over a 10 min period during which neurons were stimulated with a 60 s burst of 10 Hz firing (in the absence of TTX). Such stimulation typically leads to exocytosis of the entire recycling pool of vesicles ([Fernandez-Alfonso and Ryan, 2008](#); [Kim and Ryan, 2010](#)) and led to a transient decrease in L/F values ([Figure 3A](#), top). However, such stimuli also caused transient changes in cytosolic pH, as previously reported ([Rossano et al., 2013](#); [Svichar et al., 2011](#); [Zhang et al., 2010](#)) ([Figure 3A](#), top), which accounted for all of the activity-driven transient change in luminescence measured ([Figure 3A](#), middle).

Measurements from large numbers of cells revealed that such substantial AP firing had little impact on $\text{ATP}_{\text{presyn}}$ during the stimulus (Figure 3A, bottom) (an average decrease in ATP over the 1 min stimulus period, $^{\text{stim}}\Delta\text{ATP}_{\text{presyn}} = 0.012 \pm 0.070$ mM; $n = 30$, Figure 3B, bottom) and resulted in only a small decrease in the poststimulus period ($^{\text{poststim}}\Delta\text{ATP}_{\text{presyn}} = 0.15 \pm 0.02$ mM; $n = 30$, Figure 3B, bottom, where poststim refers to the average over a 6 min poststimulation period). Thus, under our recording conditions, metabolically intact nerve terminals are quite robust to bursts of electrical activity with respect to maintenance of ATP levels. Blockade of either major ATP synthesis pathway alone, however, revealed that, despite the high concentrations of resting ATP, new synthesis of ATP is required to maintain ATP levels during stimulation. In the presence of Oligo or dGlu, electrical activity led to a significant drop in ATP (Oligo: $^{\text{stim}}\Delta\text{ATP}_{\text{presyn}} = 0.35 \pm 0.02$ mM, $n = 9$; dGlu: $^{\text{stim}}\Delta\text{ATP}_{\text{presyn}} = 0.44 \pm 0.10$ mM, $n = 21$) that recovered over the following ~ 6 min (Oligo: $<^{\text{poststim}}\Delta\text{ATP}_{\text{presyn}}> = 0.28 \pm 0.01$ mM, $n = 9$; dGlu: $<^{\text{poststim}}\Delta\text{ATP}_{\text{presyn}}> = 0.27 \pm 0.04$ mM, $n = 21$) (Figure 3B, all ATP measurements were corrected for pH changes measured under identical conditions; Figure S3D). Because $\text{ATP}_{\text{presyn}}$ is unchanged by explicit electrical activity in metabolically intact nerve terminals but show deficits when either glycolysis or mitochondrial functions are impaired, these data demonstrate that electrical activity drives ATP synthesis, likely to meet the demands of synaptic function. Interestingly, in resting synapses (i.e., in TTX), perfusion of Oligo alone had negligible impact on $\text{ATP}_{\text{presyn}}$ (Figure 3C, top). In contrast, introduction of dGlu alone in TTX led to a continuous pronounced decline in $\text{ATP}_{\text{presyn}}$ with a $t_{1/2} = 38 \pm 8$ min (Figure 3C, middle). Thus, in the absence of electrical activity, glycolysis is necessary to support maintenance of ATP levels (Figure 3C, bottom), but both glycolysis and mitochondrial function are required to satisfy activity-dependent ATP needs.

Vesicle Cycling Consumes Most Presynaptic ATP

Following acute electrical activity, a number of ATP-consuming steps are engaged that can be parsed into three distinct, experimentally separable categories. The first category encompasses the energy needed to restore the Na^+/K^+ gradients that would be altered following AP firing, via the Na^+/K^+ ATPase. The second category consists of the energy consumed as a result of downstream calcium signaling and the need to restore intracellular Ca^{2+} levels. We treat one of the processes driven by calcium signals as the third category: exocytosis of synaptic vesicles and the ensuing synaptic vesicle cycle (Dittman and Ryan, 2009). AP firing in the absence of external calcium should only result in triggering the first category of ATP consumption, whereas AP firing in neurons that lack the ability to exocytose would eliminate the third category. Exocytosis relies on the correct assembly of SNARE proteins and can be completely eliminated at synapses by removal of the SNARE-associated protein Munc13 (Varoqueaux et al., 2002). We repeated experiments monitoring $\text{ATP}_{\text{presyn}}$ during AP firing in the presence of dGlu or Oligo but in the absence of external Ca^{2+} (Figure 4A). Stimulation in the absence of external Ca^{2+} led to much smaller changes in ATP levels compared to control in either dGlu ($^{\text{stim}}\Delta\text{ATP}_{\text{presyn}} = 0.15 \pm 0.08$ mM ($n = 9$), $<^{\text{poststim}}\Delta\text{ATP}_{\text{presyn}}> = 0.02 \pm$

0.04 mM) or in Oligo ($^{\text{stim}}\Delta\text{ATP}_{\text{presyn}} = 0.09 \pm 0.09$ mM ($n = 9$), $<^{\text{poststim}}\Delta\text{ATP}_{\text{presyn}}> = 0.05 \pm 0.04$ mM, $n = 9$) (Figure 4D). These experiments revealed that any ATP consumed by the Na^+/K^+ ATPase alone represents a relatively small energy burden compared to downstream processes at presynaptic terminals and can be met even during acute ATP synthesis blockade. Expression of an shRNA targeting the major cortical neuronal isoforms Munc13-1 and Munc13-2 led to a 94% depletion of this protein at nerve terminals that resulted in a complete block of exocytosis without significantly impacting Ca^{2+} influx during the stimulation protocols used here (Figures S4A–S4E). Measurements of $\text{ATP}_{\text{presyn}}$ in neurons expressing this shRNA revealed that resting ATP levels had more than doubled to 3.4 mM ($n = 50$) (Figure 4B). Similar results were obtained in neurons where exocytosis was alternatively eliminated by expression of the tetanus-toxin light chain (TeNT LC) (Figures S4C, S4D, and S4F). These data reveal several important unexpected features: (1) they suggest that the vesicle cycle likely presents a major ATP burden at synapses; (2) they indicate that the rate of ATP production was not downregulated in the absence of any exocytosis; and (3) they indicate that any possible negative feedback control was not sufficient to prevent elevations in ATP in the absence of this source of ATP consumption. Our earlier analysis indicated that AP firing likely leads to the stimulation of ATP production. Our measurements in Munc13 KD neurons are performed following chronic removal of Munc13 in small numbers of neurons embedded in otherwise electrically active networks, over an 8 to 11 day period. During that period, the network activity is likely quite robust. Given that electrical activity stimulates ATP production, we wondered whether elimination of AP firing in Munc13KD neurons would reduce the otherwise elevated ATP levels. To test this hypothesis, we incubated neurons that lacked Munc13 in TTX to block any network-driven or spontaneous AP firing for 7 to 9 days prior to measuring $\text{ATP}_{\text{presyn}}$. Although chronic incubation in TTX resulted in a small increase in ATP levels in WT neurons (WT + TTX: $\text{ATP}_{\text{presyn}} = 1.69 \pm 0.82$ mM, $n = 23$) compared to controls ($p = 0.04$), chronic blockade of AP firing in Munc13 KD neurons restored $\text{ATP}_{\text{presyn}}$ to levels equivalent to WT neurons treated with TTX (Munc13 KD+TTX neurons: $\text{ATP}_{\text{presyn}} = 1.67 \pm 0.97$ mM, $n = 18$) (Figures 2A and 4B). These experiments strongly imply that the synaptic vesicle cycle presents a major ATP burden in nerve terminals and that electrical activity stimulates ATP synthesis. We examined the time course of $\text{ATP}_{\text{presyn}}$ in Munc13 KD neurons treated with dGlu or Oligo and stimulated acutely with a burst of AP firing (Figure 4C). These experiments showed that in the absence of the synaptic vesicle cycle the ATP deficits observed during stimulation in either dGlu ($^{\text{stim}}\Delta\text{ATP}_{\text{presyn}} = 0.57 \pm 0.12$ mM [$n = 24$]) or Oligo ($^{\text{stim}}\Delta\text{ATP}_{\text{presyn}} = 0.34 \pm 0.16$ mM [$n = 13$]) were similar to that observed in WT synapses. However, the ATP deficits in the poststimulus period were no longer significantly different than baseline (Figure S3E; also see Experimental Procedures) in either dGlu ($<^{\text{poststim}}\Delta[\text{ATP}]_{\text{presyn}}> = 0.04 \pm 0.05$ mM) or Oligo ($<^{\text{poststim}}\Delta[\text{ATP}]_{\text{presyn}}> = 0.13 \pm 0.08$ mM) (Figure 4D). These data are consistent with the notion that many calcium-driven processes other than the synaptic vesicle cycle are responsible for the significant acute ATP consumption, but that the synaptic vesicle cycle presents a significant prolonged ATP burden at

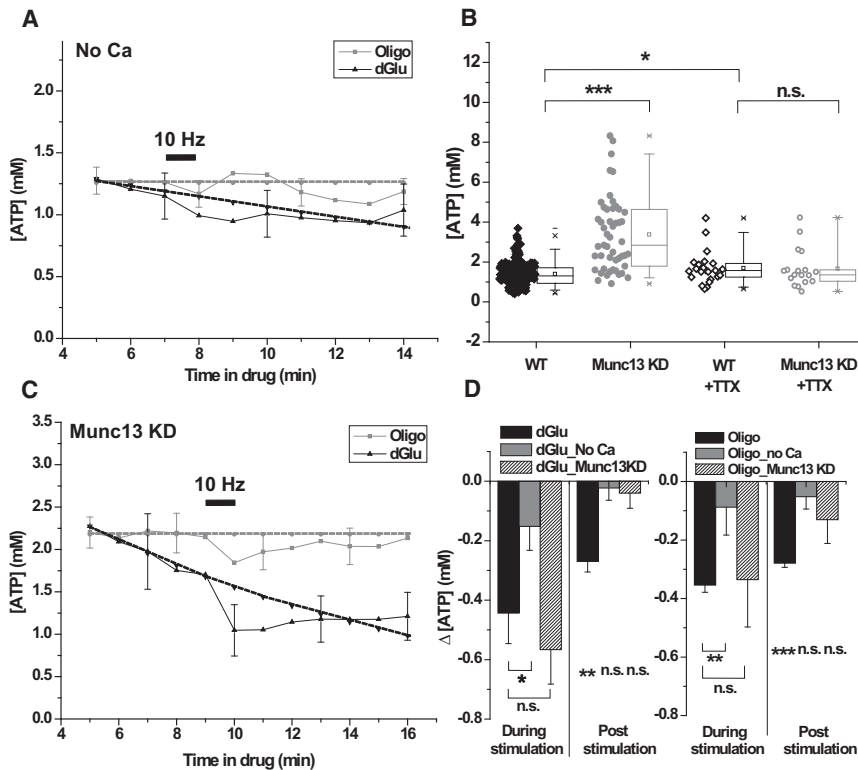


Figure 4. The Vesicle Cycle Presents a Large Presynaptic ATP Burden

(A and C) Average $[ATP]_{presyn}$ dynamics in response to 600 AP (10 Hz) in the presence of dGlu or Oligo with (A) zero external Ca^{2+} , $n = 9$ (dGlu), $n = 9$ (Oligo) and (C) in Munc13 KD neurons, $n = 8$ (dGlu), $n = 13$ (Oligo). Black dotted lines represent extrapolated baseline in the absence of stimulation and gray dotted lines represent baseline average of first 3 min (for A) and 5 min (for C) during the prestimulation period (see Experimental Procedures).

(B) Resting ATP_{presyn} was elevated in Munc13 KD compared to WT neurons ($p < 0.000001$). Chronic TTX treatment of Munc13 KD and WT, however, eliminated any differences ($p = 0.94$), whereas WT treated with TTX showed a modest increase in ATP_{presyn} values compared to WT neurons ($p = 0.04$), same as in Figure 2A. The box whisker plot represents median (line), mean (point), 25th–75th percentile (box), 10th–90th percentile (whisker), 1st–99th percentile (X), and min-max (–) ranges.

(D) Average drop in ATP_{presyn} (ΔATP_{presyn}) during the stimulus period (During stimulation) or subsequent 6 min poststimulus period (post-stimulation) in the presence of dGlu (left) or Oligo (right) for the conditions shown in (A, C, and Figure 3B) show that ATP depletion monitored during stimulation is smaller in the absence of extracellular Ca^{2+} ($p = 0.03$, dGlu, $n = 9$ and $p = 0.008$, Oligo, $n = 9$), whereas the ΔATP_{presyn}

measured in the poststimulation period was not statistically significant from its respective baselines either in the absence of external Ca^{2+} ($p = 0.7$, dGlu, $n = 9$ and $p = 0.1$, Oligo, $n = 9$) or upon removal of Munc13 ($p = 0.7$, dGlu, $n = 24$ and $p = 0.06$, Oligo, $n = 13$). Error bars are SEM. Student's *t* test was used to determine statistical significances. See also Figure S4.

nerve terminals. Both periods of ATP consumption are normally met by stimulus-dependent ATP synthesis.

Activity-Driven ATP Synthesis Required for Synaptic Function

When glycolysis was interrupted by exchanging glucose for dGlu (without TTX), ATP_{presyn} declined slowly ($t_{1/2} \sim 26$ min, Figure S3E, dGlu). Stimulation at early times under these conditions resulted in an additional drop in ATP_{presyn} (Figure 3B, middle). We wondered to what degree presynaptic function would be compromised when it could no longer rely on activity-driven glycolysis. To examine this issue, we used vGlu-pHluorin (vG-pH) to examine the balance of exo-endocytosis in response to brief bursts of APs (100 AP, 10 Hz) before and after ~ 5 min incubation in dGlu (Figure 5A). Prior to incubation in dGlu, AP firing led to a burst of exocytosis followed by endocytic retrieval and reacidification of vG-pH with a time constant of ~ 7 s (Armbruster et al., 2013; Balaji et al., 2008). After incubation in dGlu, ATP levels decreased only on average by $18\% \pm 2\%$ (to 1.14 ± 0.1 mM, Figure 3B, middle). Blockade of glycolysis at these early times, however, was accompanied by significant changes in at least two different aspects of presynaptic function: in the presence of dGlu, the vG-pH fluorescence peak at the end of the stimulus increased by 50% (Figure 5B) consistent with the dramatic reduction in endocytosis evidenced by the progressive block of recovery of the pHluorin signal following stimulation in dGlu

(pHluorin-based measurements report the balance of exocytosis and endocytosis at any given time) (Figure 5C). The elevated fluorescence signal long after the end of the stimulus was due to stranding of a significant fraction of the recently exocytosed vG-pH molecules on the synaptic surface, because this signal could be quenched by application of membrane-impermeant low-pH buffer (Figure S5A). Third, the remaining vesicles (either those that did manage to get endocytosed, or those in a nonexocytosed pool) became alkaline over the time course of the experiment shifting from an initial pH value ~ 5.6 to ~ 6.4 (Figure 5D). Similar results were obtained following simple removal of glucose (Figures S5B–S5D). Experiments using FM1-43 uptake also showed that glycolytic block resulted in a severe impairment of presynaptic function (Figures S5E and S5F). A less dramatic but still significant slowing of endocytosis was observed following 100 AP stimuli after treatment with Oligo (data not shown), whereas complete arrest of endocytosis was observed at higher stimulation conditions (600 AP) (Figures 5E–5H). All these data indicate that synapse performance is severely impaired under these conditions, suggesting that nerve terminals rely heavily on activity-stimulated ATP synthesis to maintain function.

DISCUSSION

Changes in ATP supply are thought to be linked to numerous disease states, and, given the distal location of nerve terminals with

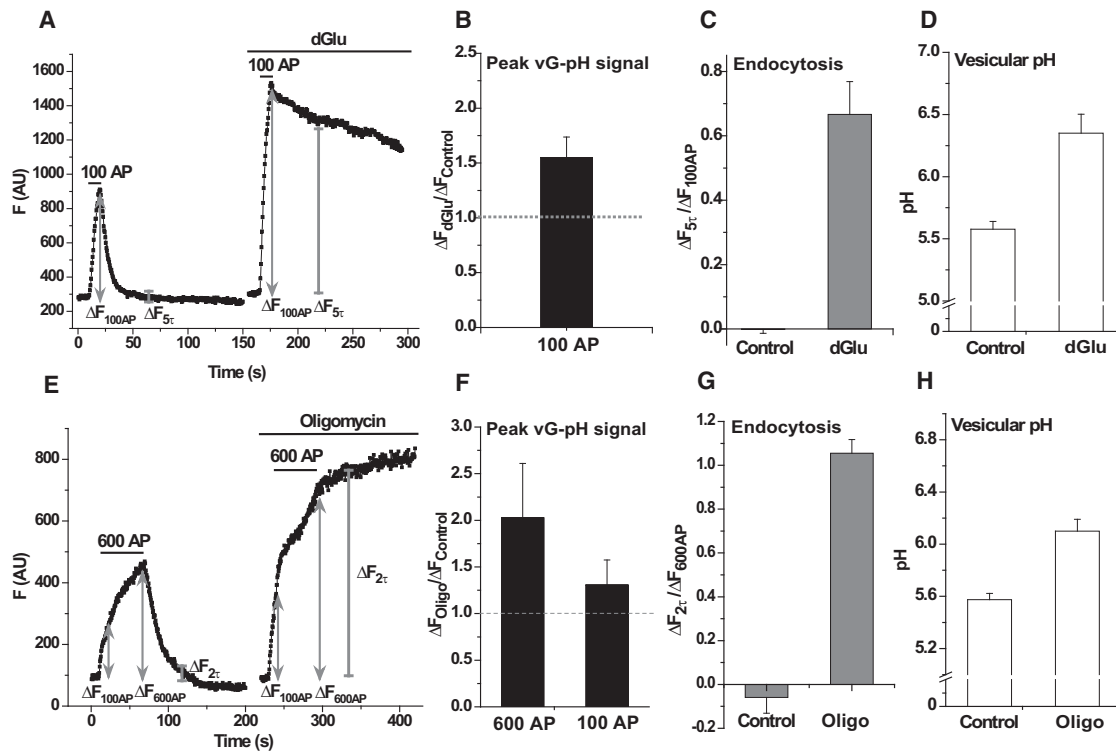


Figure 5. Presynaptic Function Relies on Activity-Driven ATP Synthesis

(A–H) Sample vGluT-pHluorin (vG-pH) traces showing (A) 100 AP responses before and after 5 min incubation in dGlu and (E) 600 AP responses before and after 5 min incubation in Oligo. Average ratio of the stimulus response in (B) dGlu compared to control ($\Delta F_{dGlu}/\Delta F_{control}$) at 100 AP ($n = 9$) and (F) Oligo compared to control ($\Delta F_{Oligo}/\Delta F_{control}$) at 600 and 100 AP ($n = 4$). Average endocytic block measured as the fraction of vG-pH fluorescence remaining at (C) five endocytic time constants (5τ) of the control at the end of 100 AP in control and dGlu ($\Delta F_{5\tau}/\Delta F_{100AP}$), $n = 9$ and (G) at two endocytic time constants (2τ) at the end of 600 AP in control and Oligo ($\Delta F_{2\tau}/\Delta F_{600AP}$), $n = 4$. Average vesicular pH determined from the vG-pH responses to NH_4Cl and acid quenching in (D) dGlu ($n = 6$) and (H) Oligo ($n = 4$). Error bars are SEM. See also Figure S5.

respect to cell bodies, synapses must rely heavily on local ATP supplies making them especially susceptible to mitochondrialopathies, a suspected pathology in several neurodegenerative diseases, including Alzheimer's disease. The development of Syn-ATP has allowed us to probe several important aspects of the regulation and consumption of ATP in nerve terminals as we demonstrate: (1) activity contributes significantly to ATP consumption; (2) activity stimulates ATP synthesis; (3) the synaptic vesicle cycle presents a large burden to ATP supplies at presynaptic sites contrary to expectations (Harris et al., 2012). Activity-driven glucose utilization is the primary signature of functional positron emission tomography-based brain imaging (e.g., using fluorodeoxyglucose), but the processes responsible for this increased metabolic need, how these changes compare to baseline metabolism, and even the cell type in which these energy demands are paramount have been difficult to dissect. Our results provide a compelling case that considerable metabolic demand is presynaptic in origin although a full accounting of the contributions from different cellular regions (e.g., dendritic postsynaptic signaling) and other cell types (e.g., astrocytes, vascular endothelia) will ultimately be required to fully understand the metabolic origin of functional brain imaging modalities. Astrocytes, in particular, have been implicated in providing

glycolytic support via an astrocyte-neuron lactate shuttle (Magistretti, 2006). At present, the role of this putative glycolytic support in our system remains to be tested; however, the ability to measure ATP in a cell-specific and subcellularly targeted fashion should now make this possible.

One of the important cell physiological questions is precisely how electrical activity leads to the stimulation of ATP synthesis through both glycolysis and oxidative phosphorylation. A primary candidate is intracellular Ca^{2+} flux. Stimulus-driven mitochondrial ATP synthesis following mitochondrial Ca^{2+} accumulation has been demonstrated in cardiomyocytes (Jouaville et al., 1999). Ca^{2+} is known as an activator of various dehydrogenases of the TCA cycle and regulates various processes of oxidative phosphorylation in the mitochondria (Balaban, 2009; Denton, 2009; Gnanapavan and Balaban, 2012), suggesting that Ca^{2+} could be one of the regulators of activity-driven ATP synthesis at nerve terminals.

Metabolic Burden versus Metabolic Sensitivity

Our finding that presynaptic function becomes severely impaired when routes of ATP synthesis are compromised suggests that the sensitivity of cognitive function to metabolic perturbations likely originates at least in part from the steep needs of nerve

terminals for activity-driven ATP synthesis and that the K_m values for ATP of certain presynaptic processes are relatively close to resting ATP levels. It is important, however, to distinguish the difference between what processes create the greatest metabolic burden versus those that create the greatest metabolic vulnerability. Processes that consume large amounts of ATP may have large safety factors and continue to operate unabated even when ATP synthesis is compromised. However, the operation of these processes under such conditions will begin to impact ATP levels, and any process whose K_m for ATP binding is closer to resting values will be impacted. Our experiments indicate that endocytic retrieval of synaptic vesicle components is one such ATP-sensitive process. Exocytosis, in contrast, although likely requires ATP for synaptic vesicle priming for example, was not immediately impacted by compromising ATP synthesis. Interestingly, endocytic machinery have recently been linked to amyloid-beta pathology (Cirrito et al., 2008), suggesting its potential link with mitochondrial dysfunction. At present the ATP-sensitive step(s) that lead to the arrest of endocytosis when ATP supply is compromised is unknown; however, one candidate for this is the mechanochemical enzyme dynamin that mediates the membrane fission step. This enzyme depends cooperatively on GTP, which, in turn, is synthesized using ATP. Interestingly nucleoside diphosphate kinase, one of the enzymes responsible for GTP synthesis was identified in an enhancer screen for modifiers of the *shibire* mutant in *Drosophila* (Krishnan et al., 2001), indicating that compromises in ATP supply may translate directly into compromises in GTP levels that, in turn, impact endocytosis. The changes in ATP levels additionally caused synaptic vesicles to become more alkaline, which is consistent with the fact that the V-type ATPase responsible for synaptic vesicle reacidification has two apparent K_m values for ATP, one of which is ~ 2 mM (Hicks and Parsons, 1992). All of these results imply that pathological states that compromise ATP supply will have profound impact on synaptic efficacy.

The results we present here establish several key principles regarding synaptic function: in metabolically intact synapses the ATP needs of presynaptic function are well matched to the activity-driven stimulation of ATP production. This stimulation of ATP synthesis likely occurs in part via a feedforward stimulation of both glycolysis and oxidative phosphorylation by electrical activity-driven calcium influx. These studies thus open up many relatively unexplored questions regarding synaptic metabolism. The approach provided here, we expect, will additionally prove useful in understanding how various disease states might impact the feedback loop that couples electrical activity at synapses with ATP synthesis and ultimately help pinpoint new therapeutic targets in neuronal dysfunction.

EXPERIMENTAL PROCEDURES

Animals

Animal experiments were performed according to procedures approved by the Weill Cornell Medical College IACUC.

Plasmid Constructs

All luciferase plasmids were constructed in a pcDNA3 vector (Invitrogen). For the construction of the chimeric Synaptophysin-mCherry-Luciferase (Syn-ATP) construct, synaptophysin was inserted between BamH1 sites and the

mcherry-luciferase chimeric sequence, separated by Age I sequence, was inserted between EcoRV and NotI sites. The variants of Syn-ATP were constructed by replacing WT luciferase in the chimera with the following mutations: TS – T214A, A215L, I232A, F295L, and E354K; K_{cat} – I423L and D436G. Luciferase TS construct was obtained from Branchini BR (Branchini et al., 2007) and the additional point mutations were incorporated by site-directed mutagenesis using PCR.

Cell Preparation, Transfection, and Imaging Setup

CA1–CA3 hippocampal regions of 1- to 3-day-old Sprague-Dawley rats were dissected, dissociated, and plated on polyornithine coated coverslips as described before (Ryan, 1999). All transfections were done using calcium-phosphate precipitation, 8 days after plating and imaging performed 13–25 days after plating. Coverslips were mounted on a laminar-flow perfusion and stimulation chamber of volume ~ 75 μ l. Action potentials were evoked by passing 1 ms pulses, yielding fields of ~ 10 V/cm across the chamber via platinum-iridium electrodes. All experiments were performed at a clamped temperature of 37°C using a custom-built objective heater under feedback control, unless otherwise mentioned. For most experiments, cells were continuously perfused at 0.1–0.2 ml/min in Tyrodes buffer containing (in mM) 119 NaCl, 2.5 KCl, 2 CaCl₂, 2 MgCl₂, 25 HEPES (buffered to pH 7.4 at 37°C), 30 glucose, 10 μ M 6-cyano-7-nitroquinoxaline-2, 3-dione (CNQX), and 50 μ M D,L-2-amino-5-phosphonopivalic acid (APV). For luminescence measurements, cells were incubated in 2 mM luciferin made in Tyrodes buffer and were replaced with fresh buffer every 10 min without additional perfusion. Unless otherwise noted, all chemicals were obtained from Sigma. Beetle luciferin, potassium salt was obtained from Promega. NH₄Cl solutions for pHluorin experiments contained (in mM) 50 NH₄Cl, 70 NaCl, 2.5 KCl, 2 CaCl₂, 2 MgCl₂, 25 HEPES, 30 glucose, 10 μ M CNQX, and 50 μ M APV. For acid quench in vG-pH experiments, solutions were made at pH 5.5 with MES replacing HEPES in Tyrodes. For FM1–43 dye (Invitrogen) experiments, 15 μ M dye made in regular Tyrodes or in dGlu was loaded onto cells and 1 mM ADVASEP made in Tyrodes buffer lacking Ca²⁺ was used for the washing step. For Fluo5F (Invitrogen) experiments, cells were transfected with VAMP-mCherry as a marker for presynaptic terminals and were loaded with ~ 7 μ g/ml Fluo5F for 10 min at 30°C, followed by a 10 min wash in Tyrodes at 30°C and a second 10 min wash at 37°C, and imaged. pH measurements using Nigericin were performed by treating cells in 20 μ M Nigericin (Molecular probes) made in modified Tyrodes buffer lacking Na⁺ and Ca²⁺ (30 mM Glucose, 2 mM MgCl₂, 123.5 mM KCl, 25 mM HEPES, 10 μ M CNQX, 50 μ M APV) buffered to pH 7.4 with KOH.

Optical Measurements and Analysis

Live-cell imaging was performed using a custom-built laser illuminated epifluorescence microscope with an Andor iXon+ (model #DU-897E-BV) back-illuminated electron-multiplying charge-coupled device camera. The camera was selected for ultralow dark noise that was further reduced by water cooling to -95°C . Fluorescence imaging was performed by illuminating cells with a 532 nm line that was rapidly shuttered using Acousto-optic Tunable Filter (AOTF). For luminescence measurements, the 532 nm laser was blocked with an external shutter and luminescent photons were collected by accumulating the image for 60 s (unless otherwise specified) in the presence of 2 mM luciferin. Continuous switching between fluorescence and luminescence image acquisitions was achieved by a custom-written Andor Basic program to control the external shutter and the AOTF as desired. All images were acquired through a 40 \times 1.3 NA Fluar Zeiss objective using a 527–537 nm excitation (for fluorescence) and 545 LP emission dichroic filters (Chroma) (for fluorescence and luminescence). Laser power at the back aperture was ~ 0.35 mW.

Images were analyzed in Image J using a custom-written plugin. Regions of Interest (ROIs) of ~ 2 μ m diameter were selected to obtain fluorescence and luminescence values of the corresponding varicosities from the respective images.

Deoxyglucose and Oligomycin Experiments

Prior to imaging, neurons were preincubated in dGlu (where 30 mM dGlu substituted for 30 mM glucose), 1 μ M Oligo (in Tyrodes buffer), or a combination of the two for 5 min. Zero Ca²⁺ buffer consisted of 4 mM MgCl₂ in dGlu or in the presence of Oligo in Tyrodes.

Munc13 KD

ShRNA construct for Munc 13-1 and -2 isoforms were made by ligating 60-mer synthetic oligonucleotides containing the rat cDNA target sequence of CCAG AGCTTTGAGATCATC (Invitrogen) into pSUPER.basic vector (OligoEngine, VEC-PBS-0002) using manufacturer's instructions. Transfection of hippocampal neurons with the shRNA constructs was performed as described above.

For TTX experiments in Munc13KD neurons, 1 μ M TTX was added to the cell media after transfection on the eighth day and imaged between 14 and 16 days after plating.

Munc13 KD Immunostaining

After live-cell imaging, Munc13 KD neurons were fixed with 4% paraformaldehyde, permeabilized with 0.2% Triton X-100, blocked with 5% BSA, and incubated with primary antibody anti-Munc13-1 rabbit (Synaptic Systems) followed by secondary antibody Alexa-488 anti-rabbit IgG (Invitrogen). Immunofluorescence images were acquired by illuminating using a fluorescence arc lamp (X-Cite 120) and 500–550 nm emission and 495 nm dichroic filters for Munc13 and 573–648 nm emission and 565 nm dichroic filters for mCherry.

Permeabilization Experiments

Cells were permeabilized by incubation with 1 U/ml Streptolysin-O (Murex Biotech) for 1–2 min in a permeabilization buffer containing 139 mM KCl, 20 mM PIPES (buffered to pH 7.0 at 37°C), 5.22 mM MgCl₂, 0.186 mM CaCl₂, and 0.91 mM EGTA (Mozhayeva et al., 2004). EGTA, MgCl₂, and CaCl₂ concentrations used were calculated to achieve free Ca²⁺ concentration of 100 nM (Tsien and Pozzan, 1989). For the ATP titration curve, permeabilized cells were incubated with ATP concentrations ranging from 0.1 to 5 mM in the presence of 2 mM luciferin at pH 7.0, 37°C. The ATP titration curve was fit to Michaelis-Menten equation.

Ca²⁺ and pH Dependence of Syn-ATP

Ca²⁺ calibration was done in the presence of 2 mM luciferin, 1 mM ATP at pH 7.0. Free Ca²⁺ concentrations of 0.1 μ M, 0.5 μ M, and 1 μ M were achieved by varying the EGTA, MgCl₂, and CaCl₂ concentrations as described (Tsien and Pozzan, 1989). For pH calibration, L/F values were measured in buffers of various pH values in the presence of luciferin, ATP, and free Ca²⁺ concentrations at 2 mM, 1 mM, and 100 nM, respectively. MES buffer was used for pH 5 and 5.5, PIPES for 6, 6.2, 6.5, 6.8, and 7, and Tris-Base for pH 7.5, 8, and 8.5. pH dependence of K_m and L/F_{max} was performed by measuring the ATP titration curve at pH 6.5 and 7.5 using PIPES and Tris-Base buffers, respectively.

Estimates of ATP Consumption by Syn-ATP

We have calibrated our EMCCD to provide a conversion between pixel intensity and number of photons per pixel. Our luminescence measurements using Syn-ATP corresponds to a total photon flux integrated over the area of a bouton of ~280 photons/min. Considering ~66% loss in photon collection efficiency due to the optical path and knowing that the published quantum yield for luciferase is 0.41, under our recording conditions we are consuming ~2,300 ATPs/min/bouton, which is much smaller than our estimates of the resting ATP levels (~10⁶/bouton).

Munc13 KD Quantification

Expression levels were quantified by selecting regions of interest (ROIs) located by mCherry signal from Syn-ATP expression representing synaptic boutons followed by measuring Munc13 immunofluorescence intensity at the same ROIs after background subtraction. The average Munc13 fluorescence intensities measured in mCherry-positive, transfected, synaptic boutons (F_{trans}) and the average Munc13 fluorescence intensities measured in mCherry-negative, untransfected, synaptic boutons (F_{untrans}) were obtained from the same illumination field. Knockdown percentage was calculated as F_{trans}/F_{untrans}.

Luciferin Impact on Synaptic Function

These experiments were performed using a Synaptophysin-mOrange-luciferase reporter where mOrange (mOr2) was tagged to the luminal side of Synaptophysin. mOr2 is pH sensitive with a pK_a of 6.5 (Shaner et al., 2004) providing a pH-sensitive reporter similar to pHluorin (Sankaranarayanan et al., 2000). Using this reporter, luciferase luminescence was monitored

simultaneously with the stimulation responses, measured by mOr2 fluorescence, at various luciferin concentrations.

Baseline Measurements

L/F measurements were made in the absence of electrical activity for Control, dGlu, dGlu in the absence of external Ca²⁺, and dGlu in Munc13 KD neurons. Corresponding pH measurements were also done at the respective conditions. In the absence of stimulation: in control, ATP levels remained constant over the duration of the time course, and in the presence of dGlu, ATP levels declined following first-order kinetics, which were fit to an exponential decay relation. The measured time constant from the exponential fits were used to extrapolate the baseline for ATP traces measured in the presence of electrical activity at respective conditions. For control and Oligo traces, the baseline averages from the prestimulation period were used to extrapolate the baseline during electrical activity.

pH Measurements

pH measurements were made using cytoplasmic pHluorin (pK_a 7.1) transfected into neurons and imaged at presynaptic varicosities. Cytosolic pH was determined by measuring the change in fluorescence response to brief perfusion with NH₄Cl buffer at pH 7.4 (Sankaranarayanan et al., 2000). We previously showed that such perfusion effectively equilibrates vesicular pH to 7.4 based on comparisons with direct protonophore-based pH-clamping (Fernandez-Alfonso and Ryan, 2008), allowing the estimation of resting pH value in the vesicle lumen, knowing the pK_a of cytoplasmic pHluorin. We made use of similar approaches for determining the resting cytosolic pH. Estimates of the resting cytosolic pH obtained by examining responses of cytoplasmic pHluorin to NH₄Cl gave very similar values to that obtained using protonophore-based pH clamping (Figure S3C). We therefore proceeded to the following procedure to determine the cytosolic pH using the modified Henderson-Hasselbalch equation:

$$\text{pH} = \text{pK}_a + \log \left[\frac{F - F_{\min}}{F_{\max} - F} \right],$$

where F is the fluorescence of cytoplasmic pHluorin at any given pH value and F_{min} and F_{max} are the extreme values of F at its quenched and saturated states. pK_a is pK_a of cytoplasmic pHluorin, 7.1.

The above equation can be used to calculate cytosolic pH, knowing that the pH of cytosol on NH₄Cl perfusion is 7.4.

$$\text{pH} = \text{pK}_a - \log \left[\left(\frac{1 + 10^{\text{pK}_a - 7.4}}{\frac{F_2}{F_1}} \right) - 1 \right]$$

pK_a is pK_a of cytoplasmic pHluorin, 7.1, F₂ is the fluorescence of cytoplasmic pHluorin measured at baseline, F₁ is the fluorescence of cytoplasmic pHluorin measured on NH₄Cl perfusion.

Use of a single-wavelength pH indicator for measuring dynamics assumes that the concentration of the probe is not changing during the experiment. This was verified by examining the time course of mCherry fluorescence (which is pH insensitive in these pH ranges) during identical experiments. We used absolute calibrations of our microscope (Balaji and Ryan, 2007) to determine that the number of cytoplasmic pHluorin molecules was ~640 in a typical synaptic bouton, which corresponds to ~1 μ M of probe.

pH Correction for ATP

The measured pH values were used to incorporate the impact of pH on luciferase's K_m for ATP, in converting L/F to [ATP]:

$$[\text{ATP}] = \frac{K_m \times \left(\frac{1 + 10^{\text{pK}_a - \text{pH}}}{1 + 10^{\text{pK}_a - 7.0}} \right) \times \left(\frac{L}{F} \right)}{\left(\frac{L}{F} \right)_{\max} - \left(\frac{L}{F} \right)},$$

where K_m, L/F_{max} are the Michaelis-Menten parameters obtained from the ATP titration curve—measured at pH 7.0—and pK_a refers to the pK_a of luciferase,

7.03. In order to determine the uncertainty involved in the ATP measurements, we used a standard equation for error propagation, as described in Taylor (1997).

Luciferin Titration

Measurement of the luciferin titration curve in vivo showed that 20 mM luciferin was the saturating concentration for Syn-ATP. However, the luciferin titration curve measured in permeabilized cells (in situ) reached saturation at 1 mM luciferin in the presence of 1 mM ATP (data not shown). We therefore corrected the in situ calibration curve as follows by assuming the effect of lowered luciferin is approximated by a change in the V_{\max} :

$$\text{Corrected} \left(\frac{L}{F} \right) = \left(\frac{L}{F} \right)_{\text{in situ}} \times \frac{\left(\frac{L}{F} \right)_{2 \text{ mM}}}{\left(\frac{L}{F} \right)_{\max}}$$

where $(L/F)_{\text{in situ}}$ is the L/F ratio measured in permeabilized cells at the respective ATP concentrations, $(L/F)_{2 \text{ mM}}$ is the L/F ratio at 2 mM luciferin from the luciferin titration curve measured in vivo. $(L/F)_{\max}$ is the V_{\max} of the luciferin titration curve measured in vivo.

SUPPLEMENTAL INFORMATION

Supplemental Information includes five figures and can be found with this article online at <http://dx.doi.org/10.1016/j.cell.2013.12.042>.

AUTHOR CONTRIBUTIONS

Experiments were designed by V.R. and T.A.R. The Munc13 KD vector was designed and validated by N.C. All other experiments were carried out by V.R. The manuscript was written by V.R. and T.A.R.

ACKNOWLEDGMENTS

We would like to thank G.A. Rutter for providing us with WT luciferase, B.R. Branchini for thermostable luciferase mutants, M.E. Hatten for cytoplasmic pHluorin construct, and M. Dong for the tetanus toxin light-chain construct. We are also thankful to Ricky Kwan, Yogesh Gera, and Julia Marrs for technical assistance, Ryan lab members, Timothy McGraw, and Jeremy Dittman for input and additional thanks to Jeremy Dittman for help with the graphical abstract. This work was supported by the Tri-Institutional Training Program in Chemical Biology (V.R.), McKnight Technological Innovations in Neuroscience award (T.A.R.), and funding from NINDS (T.A.R.).

Received: June 24, 2013

Revised: November 1, 2013

Accepted: December 31, 2013

Published: February 13, 2014

REFERENCES

- Armbruster, M., Messa, M., Ferguson, S.M., De Camilli, P., and Ryan, T.A. (2013). Dynamin phosphorylation controls optimization of endocytosis for brief action potential bursts. *eLife* 2, e00845.
- Balaban, R.S. (2009). The role of Ca^{2+} signaling in the coordination of mitochondrial ATP production with cardiac work. *Biochim. Biophys. Acta* 1787, 1334–1341.
- Balaji, J., and Ryan, T.A. (2007). Single-vesicle imaging reveals that synaptic vesicle exocytosis and endocytosis are coupled by a single stochastic mode. *Proc. Natl. Acad. Sci. USA* 104, 20576–20581.
- Balaji, J., Armbruster, M., and Ryan, T.A. (2008). Calcium control of endocytic capacity at a CNS synapse. *J. Neurosci.* 28, 6742–6749.
- Berg, J., Hung, Y.P., and Yellen, G. (2009). A genetically encoded fluorescent reporter of ATP:ADP ratio. *Nat. Methods* 6, 161–166.
- Branchini, B.R., Magyar, R.A., Murtiashaw, M.H., Anderson, S.M., and Zimmer, M. (1998). Site-directed mutagenesis of histidine 245 in firefly luciferase: a proposed model of the active site. *Biochemistry* 37, 15311–15319.
- Branchini, B.R., Ablamsky, D.M., Murtiashaw, M.H., Uzasci, L., Fraga, H., and Southworth, T.L. (2007). Thermostable red and green light-producing firefly luciferase mutants for bioluminescent reporter applications. *Anal. Biochem.* 361, 253–262.
- Cirrito, J.R., Kang, J.E., Lee, J., Stewart, F.R., Verges, D.K., Silverio, L.M., Bu, G.J., Mennerick, S., and Holtzman, D.M. (2008). Endocytosis is required for synaptic activity-dependent release of amyloid-beta in vivo. *Neuron* 58, 42–51.
- De Stefano, C., Milea, D., Pettignano, A., and Sammartano, S. (2006). Modeling ATP protonation and activity coefficients in NaClq and KClq by SIT and Pitzer equations. *Biophys. Chem.* 121, 121–130.
- Denton, R.M. (2009). Regulation of mitochondrial dehydrogenases by calcium ions. *Biochim. Biophys. Acta* 1787, 1309–1316.
- Dittman, J., and Ryan, T.A. (2009). Molecular circuitry of endocytosis at nerve terminals. *Annu. Rev. Cell Dev. Biol.* 25, 133–160.
- Fernandez-Alfonso, T., and Ryan, T.A. (2008). A heterogeneous “resting” pool of synaptic vesicles that is dynamically interchanged across boutons in mammalian CNS synapses. *Brain Cell Biol.* 36, 87–100.
- Fraga, H. (2008). Firefly luminescence: a historical perspective and recent developments. *Photochem. Photobiol. Sci.* 7, 146–158.
- Fujii, H., Noda, K., Asami, Y., Kuroda, A., Sakata, M., and Tokida, A. (2007). Increase in bioluminescence intensity of firefly luciferase using genetic modification. *Anal. Biochem.* 366, 131–136.
- Glancy, B., and Balaban, R.S. (2012). Role of mitochondrial Ca^{2+} in the regulation of cellular energetics. *Biochemistry* 51, 2959–2973.
- Granseth, B., Odermatt, B., Royle, S.J., and Lagnado, L. (2006). Clathrin-mediated endocytosis is the dominant mechanism of vesicle retrieval at hippocampal synapses. *Neuron* 51, 773–786.
- Harris, J.J., Jolivet, R., and Attwell, D. (2012). Synaptic energy use and supply. *Neuron* 75, 762–777.
- Hicks, B.W., and Parsons, S.M. (1992). Characterization of the P-type and V-type ATPases of cholinergic synaptic vesicles and coupling of nucleotide hydrolysis to acetylcholine transport. *J. Neurochem.* 58, 1211–1220.
- Imamura, H., Nhat, K.P., Togawa, H., Saito, K., Iino, R., Kato-Yamada, Y., Nagai, T., and Noji, H. (2009). Visualization of ATP levels inside single living cells with fluorescence resonance energy transfer-based genetically encoded indicators. *Proc. Natl. Acad. Sci. USA* 106, 15651–15656.
- Jouaville, L.S., Pinton, P., Bastianutto, C., Rutter, G.A., and Rizzuto, R. (1999). Regulation of mitochondrial ATP synthesis by calcium: evidence for a long-term metabolic priming. *Proc. Natl. Acad. Sci. USA* 96, 13807–13812.
- Kim, S.H., and Ryan, T.A. (2010). CDK5 serves as a major control point in neurotransmitter release. *Neuron* 67, 797–809.
- Krishnan, K.S., Rikhy, R., Rao, S., Shivalkar, M., Mosko, M., Narayanan, R., Etter, P., Estes, P.S., and Ramaswami, M. (2001). Nucleoside diphosphate kinase, a source of GTP, is required for dynamin-dependent synaptic vesicle recycling. *Neuron* 30, 197–210.
- Ly, C.V., and Verstreken, P. (2006). Mitochondria at the synapse. *Neuroscientist* 12, 291–299.
- Magistretti, P.J. (2006). Neuron-glia metabolic coupling and plasticity. *J. Exp. Biol.* 209, 2304–2311.
- Martys, J.L., Shevell, T., and McGraw, T.E. (1995). Studies of transferrin recycling reconstituted in streptolysin O permeabilized Chinese hamster ovary cells. *J. Biol. Chem.* 270, 25976–25984.
- Moyer, J.D., and Henderson, J.F. (1983). Nucleoside triphosphate specificity of firefly luciferase. *Anal. Biochem.* 131, 187–189.
- Mozhayeva, M.G., Matos, M.F., Liu, X., and Kavalali, E.T. (2004). Minimum essential factors required for vesicle mobilization at hippocampal synapses. *J. Neurosci.* 24, 1680–1688.

- Rossano, A.J., Chouhan, A.K., and Macleod, G.T. (2013). Genetically encoded pH-indicators reveal activity-dependent cytosolic acidification of *Drosophila* motor nerve termini in vivo. *J. Physiol.* 591, 1691–1706.
- Ryan, T.A. (1999). Inhibitors of myosin light chain kinase block synaptic vesicle pool mobilization during action potential firing. *J. Neurosci.* 19, 1317–1323.
- Saito, K., Chang, Y.F., Horikawa, K., Hatsugai, N., Higuchi, Y., Hashida, M., Yoshida, Y., Matsuda, T., Arai, Y., and Nagai, T. (2012). Luminescent proteins for high-speed single-cell and whole-body imaging. *Nat. Commun.* 3, 1262.
- Sankaranarayanan, S., De Angelis, D., Rothman, J.E., and Ryan, T.A. (2000). The use of pHluorins for optical measurements of presynaptic activity. *Biophys. J.* 79, 2199–2208.
- Shaner, N.C., Campbell, R.E., Steinbach, P.A., Giepmans, B.N.G., Palmer, A.E., and Tsien, R.Y. (2004). Improved monomeric red, orange and yellow fluorescent proteins derived from *Discosoma* sp. red fluorescent protein. *Nat. Biotechnol.* 22, 1567–1572.
- Shaner, N.C., Steinbach, P.A., and Tsien, R.Y. (2005). A guide to choosing fluorescent proteins. *Nat. Methods* 2, 905–909.
- Svichar, N., Esquenazi, S., Chen, H.Y., and Chesler, M. (2011). Preemptive regulation of intracellular pH in hippocampal neurons by a dual mechanism of depolarization-induced alkalinization. *J. Neurosci.* 31, 6997–7004.
- Tantama, M., Martinez-Francois, J.R., Mongeon, R., and Yellen, G. (2013). Imaging energy status in live cells with a fluorescent biosensor of the intracellular ATP-to-ADP ratio. *Nature communications* 4, 2550.
- Taylor, J. (1997). *An Introduction to Error Analysis: the Study of Uncertainties in Physical Measurements*, 2nd ed. (Sausalito: University Science Books).
- Tsien, R., and Pozzan, T. (1989). Measurement of cytosolic free Ca^{2+} with quin2. *Methods Enzymol.* 172, 230–262.
- Varoqueaux, F., Sigler, A., Rhee, J.S., Brose, N., Enk, C., Reim, K., and Rosenmund, C. (2002). Total arrest of spontaneous and evoked synaptic transmission but normal synaptogenesis in the absence of Munc13-mediated vesicle priming. *Proc. Natl. Acad. Sci. USA* 99, 9037–9042.
- Zhang, Z.S., Nguyen, K.T., Barrett, E.F., and David, G. (2010). Vesicular ATPase inserted into the plasma membrane of motor terminals by exocytosis alkalinizes cytosolic pH and facilitates endocytosis. *Neuron* 68, 1097–1108.

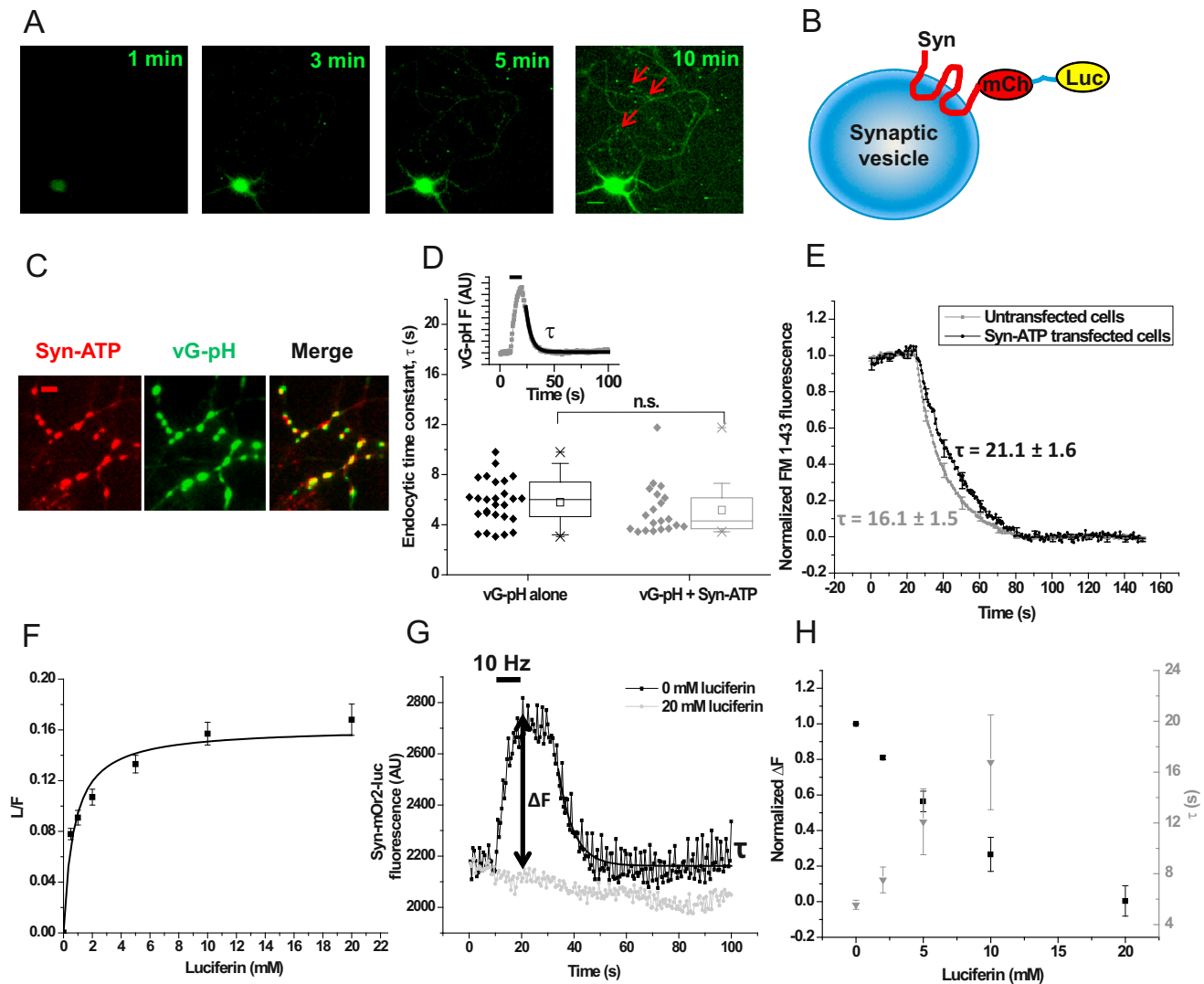


Figure S1. Imaging Syn-ATP at Synaptic Terminals, Related to Figure 1

(A) Luminescence images acquired at integration timescales of 1, 3, 5 and 10 min. Red arrows indicate putative presynaptic structures. Scale bar 20 μ m.

(B) Cartoon representation of the Syn-ATP construct expressed on a synaptic vesicle.

(C) Syn-ATP mCherry fluorescence (red), vGlut pHluorin (vG-pH) fluorescence (green) and merged (yellow) images showing colocalization of Syn-ATP with vG-pH at presynaptic terminals. Scale bar = 5 μ m.

(D) Average endocytic time constants measured in vG-pH expressing terminals, $\tau = 5.8 \pm 0.35$ s, $n = 27$, and in vG-pH coexpressed with Syn-ATP expressing terminals, $\tau = 5.2 \pm 0.45$ s, $n = 20$, showing no significant difference between the two conditions ($p = 0.28$). (inset) Sample vG-pH time trace in response to 100 AP (10 Hz) stimulation (black bar), showing exponential fit measuring the endocytosis time constant, τ . The Box whisker plots represent median (line), mean (point), 25 - 75 percentile (box), 10 - 90 percentile (whisker), 1 - 99 percentile (X) and min - max (—) ranges.

(E) Average trace showing FM1-43 unloading fit to exponential decay time constant, τ , showed minor impact on exocytosis kinetics in cells transfected with Syn-ATP ($\tau = 21.1 \pm 1.6$, $n = 8$) (black) compared to untransfected cells ($\tau = 16.1 \pm 1.5$, $n = 8$) (gray). Cells were loaded in the presence of FM1-43 during a 10 Hz for 10 s stimulus with an additional 30 s period poststimulus. Cells were then washed in ADVASEP and in the absence of Ca^{2+} to remove unbound dye, following which they were unloaded at 10 Hz 60 s stimulation while being imaged.

(F) Luciferin titration curve measured in live neurons. K_m (luciferin) = 0.71 ± 0.15 mM, V_{max} = 0.16 ± 0.009 , $n = 9$.

(G) mOrange (mOr2) fluorescence response to 10 Hz 20 s stimulation measured at 0 and 20 mM luciferin concentration. (H) Effect of luciferin on fluorescence response, ΔF and endocytic time constant, τ , $n = 4$.

Error bars are SEM.

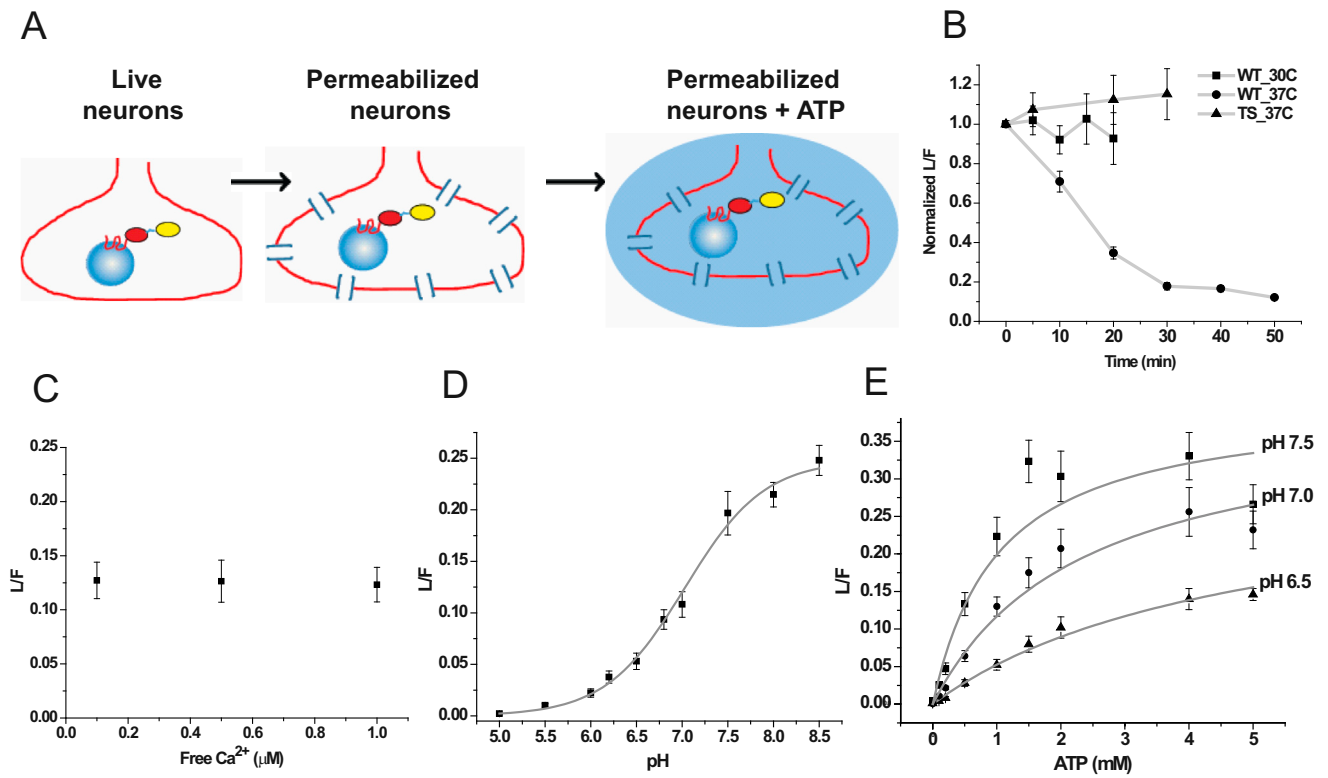


Figure S2. Calibration of Syn-ATP, Related to Figure 1

(A) Cartoon representation of the permeabilization protocol.

(B) Activity of WT and TS luciferase monitored at 30°C and 37°C in permeabilized cells.

(C) Ca^{2+} dependence of Syn-ATP, $n = 6$.

(D) pH titration curve of Syn-ATP, $\text{pK}_a = 7.03 \pm 0.04$, $n = 9$.

(E) ATP titration curve measured at: pH 7.5, $K_m = 1.0 \pm 0.4$ mM, $V_{\max} = 0.4 \pm 0.1$ ($n = 7$); pH 7.0, $K_m = 2.3 \pm 0.6$ mM, $V_{\max} = 0.4 \pm 0.1$ ($n = 10$) and pH 6.5, $K_m = 4.8 \pm 1.3$ mM, $V_{\max} = 0.3 \pm 0.1$ ($n = 7$).

Error bars are SEM.

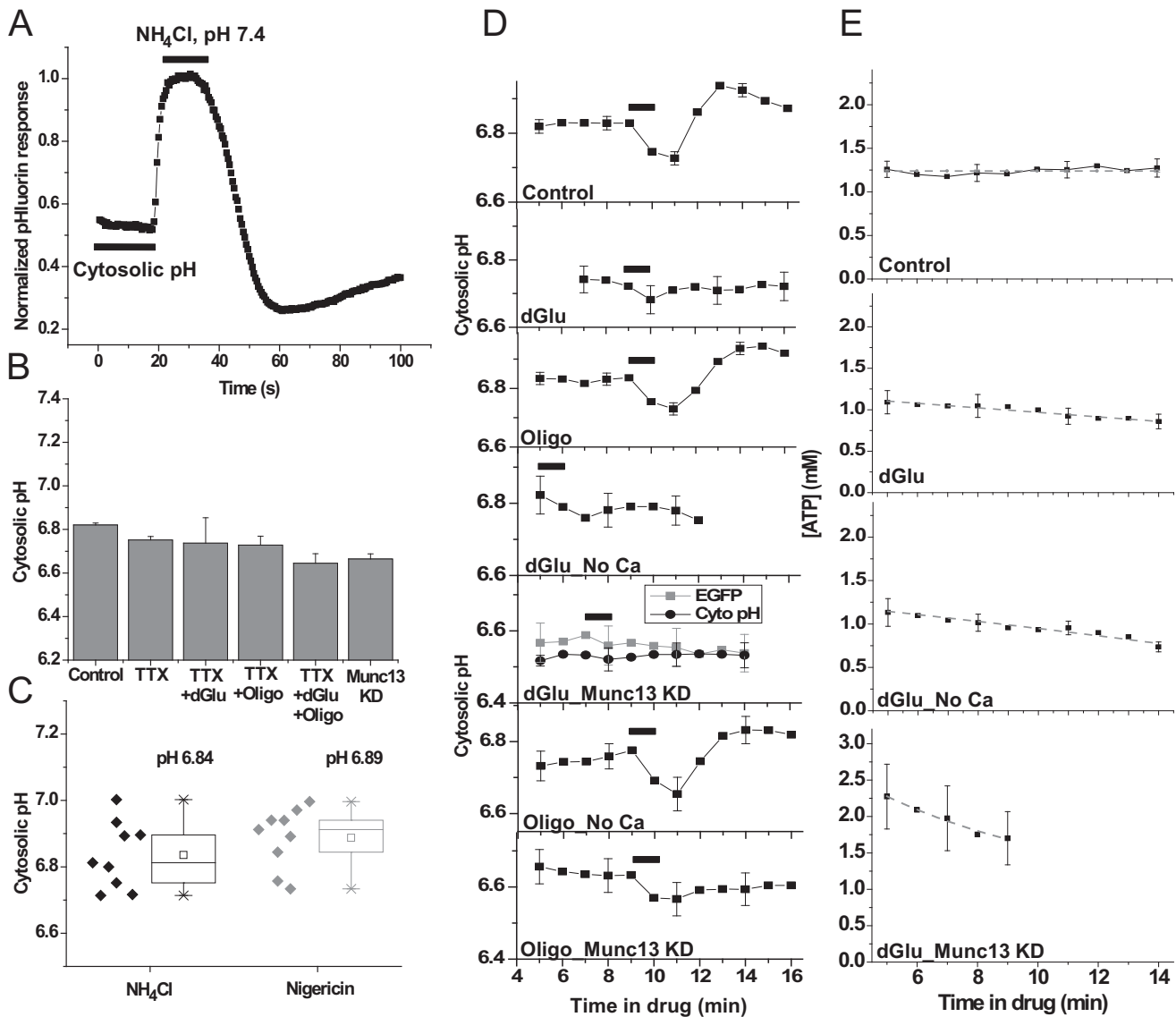


Figure S3. Cytosolic pH and Baseline ATP Measurements, Related to Figures 2 and 3

(A) Cytoplasmic pHluorin fluorescence during perfusion with NH_4Cl .

(B) Cytosolic pH measured in control (Average = 6.82 ± 0.1 , $n = 94$, CV = 1.4%), in the presence of TTX ($n = 20$), TTX + dGlu ($n = 6$), TTX + Oligo ($n = 5$), TTX + dGlu + Oligo ($n = 5$), Munc13 KD, absence of TTX ($n = 32$).

(C) Pairwise cytosolic pH measurements made in cytoplasmic pHluorin expressing synaptic terminals by either NH_4Cl perfusion ($\text{pH} = 6.84 \pm 0.03$, $n = 9$) or Nigericin-based pH clamping ($\text{pH} = 6.89 \pm 0.03$, $n = 9$). The Box whisker plots represent median (line), mean (point), 25-75 percentile (box), 10-90 percentile (whisker), 1-99 percentile (X) and min-max (—) ranges.

(D) Cytosolic pH changes measured in response to 600 AP (10Hz) stimulation (black bar) in Control, $n = 12$, dGlu, $n = 9$, Oligo, $n = 12$, dGlu and no external Ca^{2+} , $n = 6$, dGlu in Munc13 KD, $n = 10$ in comparison with pH measurements in the same condition, using EGFP as a pH reporter with a pK_a of 6.0, $n = 10$, Oligo and no external Ca^{2+} , $n = 8$ and Oligo in Munc13 KD, $n = 9$ conditions.

(E) Control, linear fit (gray dotted line) of the baseline $[\text{ATP}]_{\text{presyn}}$ measurement in the absence of electrical activity, $n = 20$, dGlu, exponential fit (gray dotted line), exponential time constant (τ) = 37 ± 5 min, $n = 11$, dGlu with no external Ca^{2+} , τ = 25 ± 2 min, $n = 6$, and dGlu in Munc13 KD neurons, τ = 13 ± 1 min, $n = 8$.

Error bars are SEM.

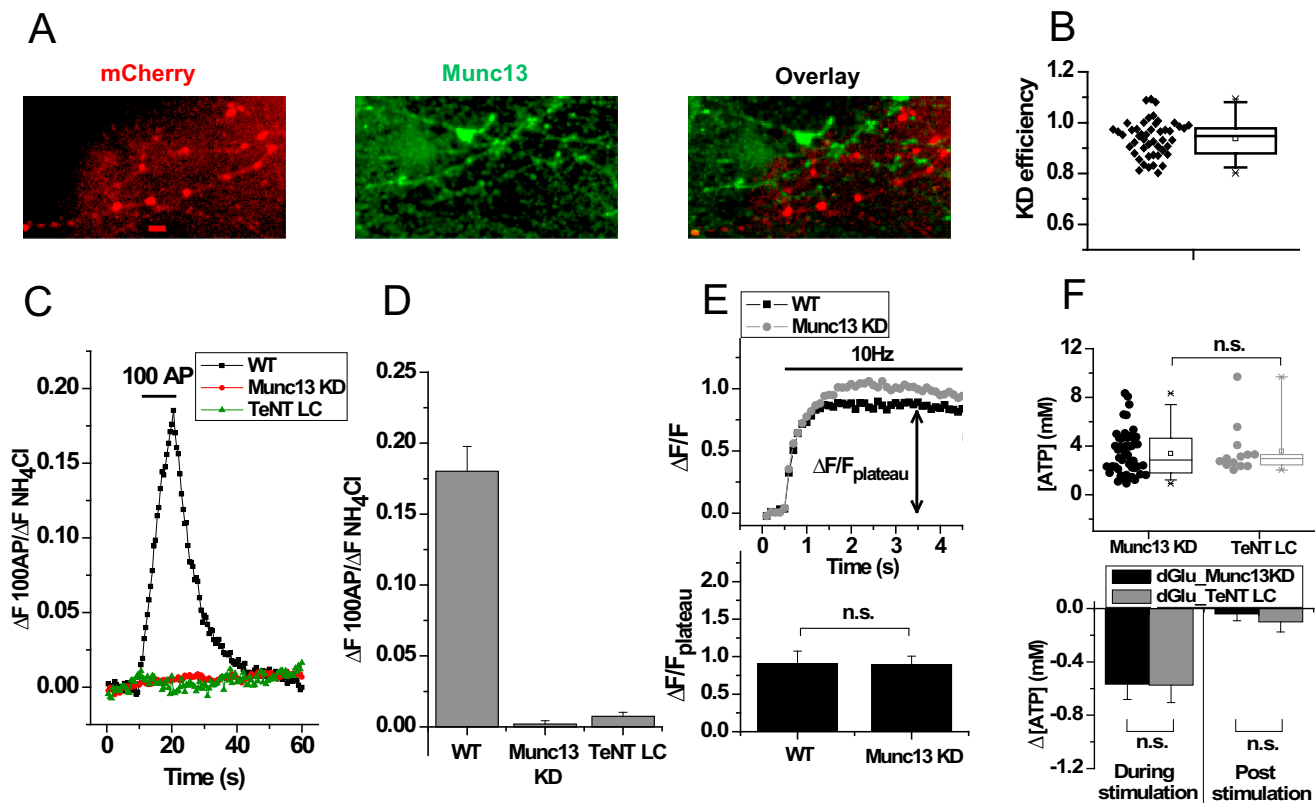


Figure S4. Munc13 Knockdown and TeNT LC Expression, Related to Figure 4

(A) mCherry fluorescence from Syn-ATP (red) in a neuron additionally transfected with an shRNA targeting Munc13-1 fixed and stained using an anti-Munc13-1 antibody and visualized with an Alexa-488-labeled secondary antibody (green). Syn-ATP expressing neurons did not stain for Munc13-1 suggesting efficient shRNA KD in the transfected neurons, whereas the adjacent untransfected neurons not expressing Syn-ATP or the shRNA stained for Munc13-1. Scale bar 5 μ m.

(B) Munc13-1 knockdown efficiency measured at the cell soma from 48 different neurons expressing the shRNA compared to the average cell somas of non-transfected cells in the field of view. Mean KD efficiency = $0.94 \pm 0.01\%$.

(C) Sample vG-pH response to 100 AP (10Hz) stimulation in WT, Munc13 KD and TeNT LC expressing cells as a fraction of NH_4Cl response.

(D) Average vG-pH response measured across many cells, WT, $n = 24$, Munc13 KD, $n = 11$, TeNT LC, $n = 6$.

(E) (top) Sample Fluo5F Ca^{2+} response ($\Delta F/F$) to 40 AP (10 Hz) measured in WT (black) and Munc13 KD (gray) cells. Fluo5F is well below saturation for such stimulus conditions. The traces were normalized to the maximal value (in this case it was the Munc13-1 that showed a slightly higher peak). (bottom) Average change in Fluo5F fluorescence measured over the plateau (measured between $t = 2$ and $t = 4$ s) during the stimulus showed no difference between WT ($\Delta F/F_{plateau} = 0.9 \pm 0.2$, $n = 7$) and Munc13 KD ($\Delta F/F_{plateau} = 0.9 \pm 0.1$, $n = 13$) cells ($p = 0.4$).

(F) (top) Resting ATP_{presyn} measured in TeNT LC expressed cells ($ATP_{presyn} = 3.6 \pm 0.6$ mM, $n = 13$) was not significantly different from the elevated ATP levels measured in Munc13 KD neurons ($ATP_{presyn} = 3.4 \pm 0.3$ mM, $n = 50$, same as in Figure 4B) ($p = 0.73$). The Box whisker plots represent median (line), mean (point), 25-75 percentile (box), 10-90 percentile (whisker), 1-99 percentile (X), and min-max (—) ranges. (bottom) Average drop in ATP_{presyn} measured in TeNT LC expressed neurons ($n = 7$) was not significantly different from Munc13 KD neurons ($n = 8$) in the presence of dGlu, either during the stimulus period (Munc13 KD: $\Delta[ATP]_{presyn}^{stim} = 0.57 \pm 0.12$ mM (same as in Figure 4D left), TeNT LC: $\Delta[ATP]_{presyn}^{stim} = 0.57 \pm 0.13$ mM, $p = 0.97$) or subsequent 6 min poststimulus period (Munc13 KD: $\Delta[ATP]_{presyn}^{poststim} = 0.04 \pm 0.05$ mM, TeNT LC: $\Delta[ATP]_{presyn}^{poststim} = 0.10 \pm 0.08$ mM, $p = 0.46$). Error bars are SEM. Student's t test was used to determine statistical significances.

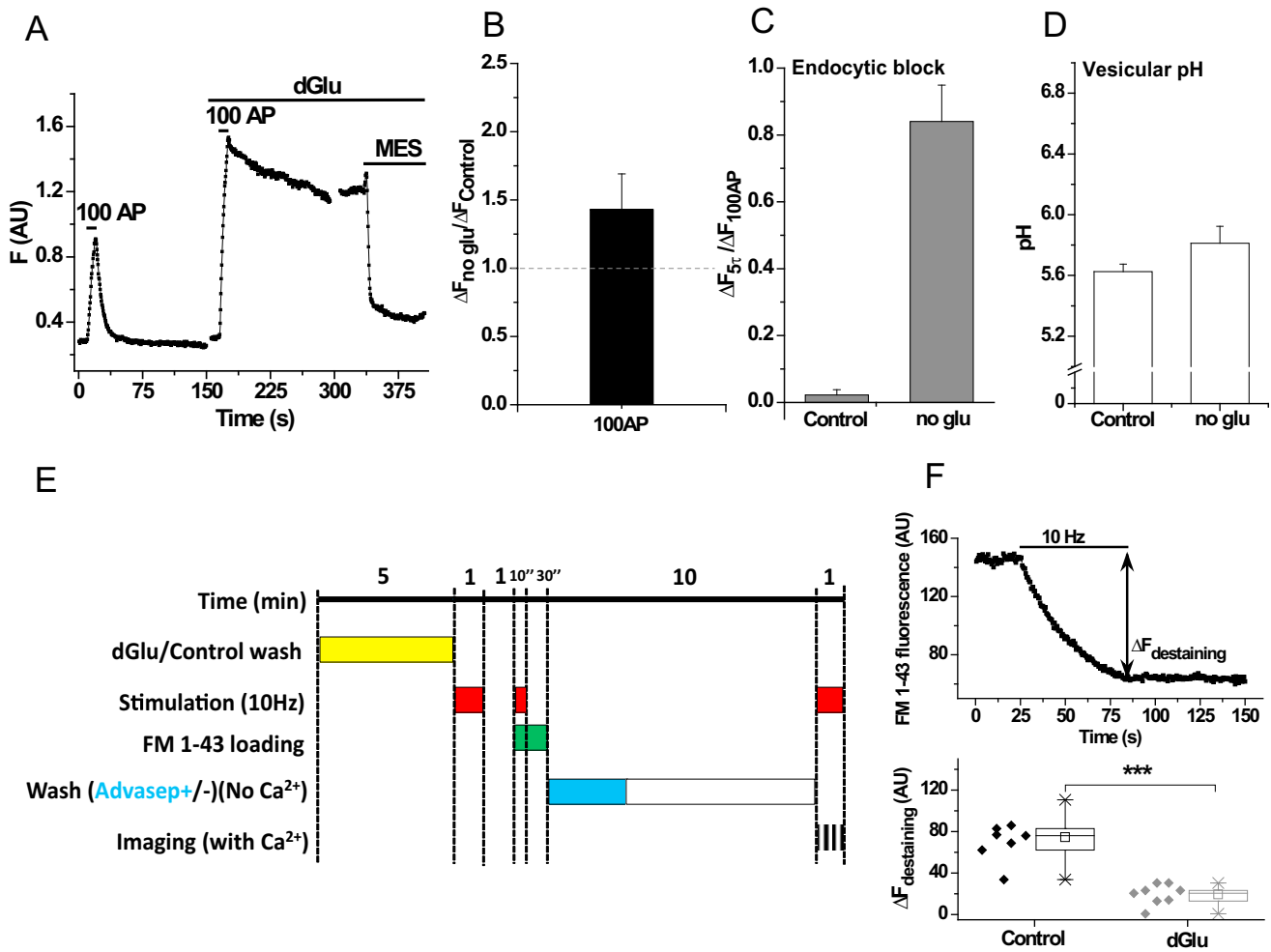


Figure S5. Impact of ATP Synthesis Block on Synaptic Function, Related to Figure 5

(A) Sample vG-pH response to 100 AP (10Hz) stimulation before and after dGlu treatment followed by acid quench using MES, pH 5.5.

(B) Average ratio of the stimulus response in the absence of glucose compared to control ($\Delta F_{\text{no glu}} / \Delta F_{\text{control}}$) at 100 AP, $n = 8$.

(C) Average endocytic block measured as the fraction of vG-pH fluorescence remaining at 5 endocytic time constants (τ) after the end of the stimulus in control and in the absence of glucose ($\Delta F_{5\tau} / \Delta F_{100\text{AP}}$), $n = 8$.

(D) Average vesicular pH determined from the vG-pH responses to NH_4Cl and acid quenching, $n = 8$ (right).

(E) Schematic diagram of FM1-43 loading experiment in control or dGlu conditions. Cells were initially washed in either regular Tyrodes or dGlu for 5 min (yellow bar) and stimulated at 10 Hz for 60 s (red bar) then stimulated a second time for 10 s at 10 Hz in the presence of FM-143 which was washed 30 s after the end of the second stimulus (green bar). Washing of FM1-43 was done in ADVASEP and in the absence of Ca^{2+} to remove unbound dye (blue/white bar). After 10 min of washing, external calcium was restored and neurons were stimulated at 10 Hz 60 s while being imaged (black striated lines) to follow FM1-43 destaining.

(F) (top) Sample trace showing FM1-43 destaining according to the protocol. (bottom) The amplitude of the destaining (ΔF) which reflects the amount of dye loaded during the stimulus in the presence of FM1-43 was ~3.8-fold lower in the presence of dGlu ($n = 8$) than in control ($n = 8$) cells ($p = 0.00001$). The Box whisker plots represent median (line), mean (point), 25-75 percentile (box), 10-90 percentile (whisker), 1-99 percentile (X), and min-max (—) ranges. Error bars are SEM.